FERMILAB-PUB-15-521-A-AD-AE-CD-PPD

Search for Space-Time Correlations from the Planck Scale with the Fermilab Holometer

Aaron S. Chou,[a] Richard Gustafson,[b] Craig Hogan,[a,c] Brittany Kamai,[c,g], Ohkyung Kwon,[c,e] Robert Lanza,[c,d], Lee McCuller,[c,d], Stephan S. Meyer,[c], Jonathan Richardson,[c] Chris Stoughton,[a] Raymond Tomlin,[a] Samuel Waldman,[f] Rainer Weiss[d]

[a] *Fermi National Accelerator Laboratory;* [b] *University of Michigan;* [c] *University of Chicago;* [d] *Massachusetts Institute of Technology;* [e] *Korea Advanced Institute of Science and Technology (KAIST);* [f] *SpaceX;* [g] *Vanderbilt University*

Measurements are reported of high frequency cross-spectra of signals from the Fermilab Holometer, a pair of co-located 39 m, high power Michelson interferometers. The instrument obtains differential position sensitivity to cross-correlated signals far exceeding any previous measurement in a broad frequency band extending to the 3.8 MHz inverse light crossing time of the apparatus. A model of universal exotic spatial shear correlations that matches the Planck scale holographic information bound of space-time position states is excluded to 4.6σ significance.

Considerations of semiclassical black hole theory suggest that quantum effects invalidate the classical gravitational theory of time and space at the Planck length, $l_P \equiv \sqrt{\hbar G/c^3}$ and that quantum states on all scales have a holographic bound on maximum information content given by areas of bounding surfaces measured in Planck units[1–4]. Effects of this limited information capacity could appear as observable exotic correlations in space-time measurements – macroscopically coherent, nonlocally correlated displacement noise in the measured positions of neighboring massive bodies. This letter reports a test of a particular model of this correlated holographic noise (cHN).

In general, exotic spacetime correlations, if they exist at all, need not behave like gravitational waves, or any perturbation of a metric or field amplitude. While no well-established quantum theory of macroscopic space predicts the exact form of these correlations, their properties are nevertheless constrained by causal structure and by the holographic information bound [5–8]. These considerations imply an irreducible transverse displacement variance $\langle x_\perp^2 \rangle \approx R l_p/\sqrt{4\pi}$ corresponding to diffraction of Planckian waves over a spatial scale R. This intrinsic noise is expected to have a nonlocal and transverse spatial structure – coherent shear or rotation simultaneously observable by co-located devices separated by distances smaller than the causal scale R.

The Fermilab Holometer utilizes a pair of large Michelson interferometers to search for shear correlations of this magnitude. The orthogonal arm configuration gives sensitivity to transverse beam splitter displacement noise which creates apparent changes in the differential arm length (DARM), i.e. $X \equiv L_1 - L_2$ where L_1, L_2 are the lengths of the two arms of a single interferometer. The cHN accrues over light travel intervals characterized by $R \approx L_1 \approx L_2 = 39.06$ m. A particular model of the cHN which saturates the Planck scale holographic information content gives the predicted power spectrum [5–7]:

$$\mathrm{PSD}_{\Delta X}(f) = \frac{l_P R^2}{\sqrt{\pi} c} \cdot \frac{\sin^2(\pi(2R/c)f)}{(\pi(2R/c)f)^2} \qquad (1)$$

which is a sinc response function normalized to $4.64\times10^{-41}\,\mathrm{m}^2/\,\mathrm{Hz}$.

Experimental design — The apparatus adopts many of the technologies of laser interferometry developed for gravitational-wave detection[9–13]. To improve sensitivity to the cHN, it implements much better time resolution and cross correlation of signals from co-located interferometers. Moreover, to maximize sensitivity to the predicted shear signals transverse to the light propagation direction, all of the laser light is concentrated on the beam splitter rather than stored in arm cavities which are sensitive only to longitudinal strain.

To perform the cross-correlation measurement, the two identical Michelson interferometers are arranged in a nested configuration with beam splitters separated by $d = 0.91$ m. A predicted decoherence due this separation scale causes a small $d/R = 2.3\%$ reduction in the normalization of the observable cHN spectrum. This spectrum can then be detected by cross-correlating the signal outputs of the two devices. The independent shot noise and all other uncorrelated noise averages away over many repeated and independent cross-spectrum measurements, leaving only the signal power which is coherent between the two data streams. A spectral analysis is then used to focus the search for a stationary cHN spectrum to high (MHz) frequencies to avoid coherent environmental (seismic, etc.) backgrounds which dominate at lower frequencies.

In each interferometer, continuous wave $\lambda = 1064\,\mathrm{nm}$ laser light is injected to a beamsplitter, divided into two orthogonal arms and reflected at distant end mirrors. The returning beams coherently interfere at the beamsplitter, with intensity varying as $P_{\mathrm{fringe}} = P_{\mathrm{BS}}(\epsilon_{\mathrm{cd}} + (1-\epsilon_{\mathrm{cd}})\sin^2(2\pi X/\lambda))$ at the antisymmetric port. P_{BS} is the power incident on the beamsplitter and the contrast defect parameter ϵ_{cd} characterizes residual leakage of non-interfering light caused by geometrical mismatches in the beams returning from the two arms. The remaining power exiting the symmetric beam splitter port and returning towards the laser is instead reflected back into

Operated by Fermi Research Alliance, LLC under Contract No. De-AC02-07CH11359 with the United States Department of Energy.

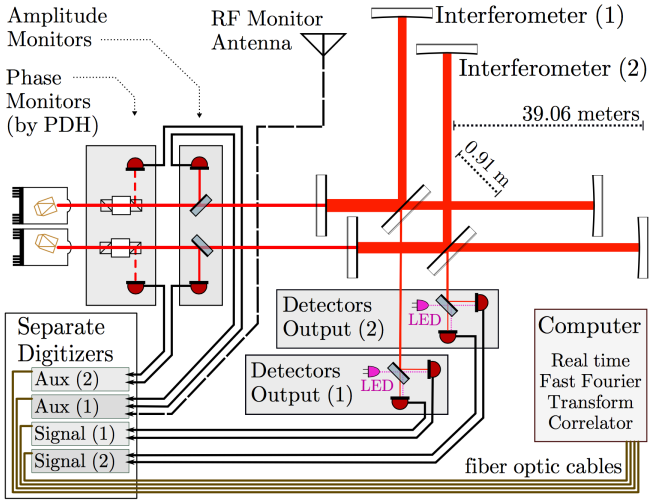

FIG. 1: Schematic of the two co-located interferometers and associated data acquisition channels. The two devices are optically and electrically isolated to eliminate cross-talk.

the device using a 1000 ppm transmission mirror. The insertion of this input coupling mirror forms a Fabry-Perot cavity with free spectral range FSR $\approx$ 3.8 MHz determined by the common arm length $(L_1+L_2)/2$. The laser is frequency-locked to the instantaneous cavity frequency via the Pound-Drever-Hall (PDH) technique [14, 15] to achieve a typical power build-up from the injected 1.1 W laser power to intracavity power $P_{\rm BS} \approx 2.2$ kW. The cavity with 650 Hz transmission bandwidth also serves to filter higher frequency amplitude and phase noise present on the incident laser beam.

To produce a linear response to differential length perturbations δX, each interferometer is operated at a DARM offset of around 1 nm from a dark fringe. A digital control system monitors fluctuations in the output light and feeds back differential signals to piezo-electric actuated end mirror mounts to hold the fringe offset to better than 0.5 Å RMS, thus maintaining a stable operating point. At this fringe offset, around 50 ppm of signal-bearing interference light appears at the anti-symmetric port, as measured relative to the intracavity power. This value is chosen to balance the interference fringe light with the the contrast defect light leakage $\epsilon_{\rm cd} \approx 50$ ppm. This non-interfering light carries no signal but contributes shot noise variance.

The shot-noise-limited displacement sensitivity is

$$\mathrm{PSD}_{\Delta X}^{\rm shot} = (\lambda/4\pi)^2 \cdot \frac{2E_\gamma}{P_{\rm BS}} \qquad (2)$$

where $E_\gamma = hc/\lambda$ is the energy per photon. Taking account of detection inefficiencies and the degradation due to the contrast defect light, the DARM sensitivity given by the 2 kW of photon power is around $(2.5\times10^{-18}\,\mathrm{m}/\sqrt{\mathrm{Hz}})^2$; this value is confirmed by calibration measurements as summarized below. To reach the predicted cHN power which is smaller by more than five orders of magnitude from the instantaneous sensitivity, the signals from the two interferometers are cross-correlated and averaged. This paper reports on 145 hours of data constituting $N > 2\times10^8$ independent spectra in each interferometer which are used to achieve a $\sqrt{N}$ improvement in sensitivity to correlated sub-shot-noise spectral power. The broadband nature of the predicted cHN allows further sensitivity improvement by searching for signal power over 2000 resolved frequency bins.

The success of the experiment requires low instrumental correlation between the two interferometers and requires nearly complete independence of the two devices, despite sharing an experimental hall. Each interferometer is enclosed in its own vacuum system, and the injection and control systems are operated on separate optics tables and electronics racks. The digitizers for the two instruments are isolated and independently synchronized to GPS. They communicate with the realtime spectrum processing computer only through optical fiber (see Fig. 1).

Data acquisition and methodology — Because of the contrast defect light leakage, each interferometer has 200 mW output power which provides the desired shot-noise-limited sensitivity. However, the large dynamic range between the DC power and the shot noise level presents challenges for linear detection. The output power is split by a secondary beam splitter to divide it between two custom low transimpedance photoreceivers based on high linearity, 2 mm InGaAs photodiodes. Each detector is demonstrated to achieve high linearity with photocurrents up to 130 mA. A low gain DC amplification channel samples the photocurrent and has flat response from DC-80 kHz. A high gain, transimpedance-based, AC-coupled radiofrequency (RF) channel has full gain between 900 kHz-5 MHz and operates up to 20 MHz.

The two interferometers together thus have four RF output streams digitized at 50 MHz sample rate with 15 bits. These four channels along with an additional four auxiliary monitor channels are Fast Fourier Transformed in real time with 381 Hz frequency resolution. An upper-triangular 8×8 cross-spectrum matrix is computed. To reduce the data rate, measurements of these 36 spectra are averaged over 700 sequential spectral measurements (around 1.8 s) before being stored. The remaining averaging is performed in offline analysis.

Isolation of the two interferometers is established by measurement; as described below, the auxiliary channels are used to determine the transfer function of known noise sources into the interferometer output, to reduce the noise coupling, and to monitor the possible remaining noise leakage in situ. During the accumulation for this result the auxiliary channels are set at various times to monitor the PDH laser phase noise, the laser intensity noise, and loop antennas detecting the local RF environment.

Absolute calibration of sensitivity — A calibration ladder is used to calibrate the instantaneous length sensitivity at MHz frequencies. Because of resonances in the piezo stacks actuating the end mirrors, a mechanical dither signal can only be injected at a low frequency of 1 kHz, whereas the RF detector channel is hi-passed at 900 kHz. The 1 kHz dither is calibrated by misaligning the cavity mirrors to operate the interferometers in a non-power-recycled configuration with a simple Michelson response. The end mirrors are then slowly actuated to sweep across an entire interference fringe to reference the voltage signal to the 1064 nm wavelength. After making corrections for the measured transfer functions of the interferometer control system, the in situ dither amplitude is determined to be 10^{-11} m. Measurements of the the low-passed DC and the high-passed RF transfer functions of the photoreceivers indicate that the calibration can be transferred to the signal band above 1 MHz with 5% systematic uncertainty. The resulting calibration is consistent with the sensitivity expected from the interferometer power level.

In situ monitoring of data quality – During data-taking operations, the 1 kHz DARM dither is run continuously. For each detector, both the DC photocurrent and the 1 kHz signal are monitored from the detector DC channel and the ratio of these measures is a proxy for the instantaneous fringe offset. The shot noise level in the 1-2 MHz signal band is also continuously monitored and the ratio of this to the DC photocurrent signal monitors the relative stability of the photoreceiver RF and DC channel responses. These and other observables such as the power reflected from the cavity back towards the laser and the power transmitted through the end mirrors serve to monitor the stability of the calibrated sensitivity of the instrument to position disturbances. The uncertainty in calibration from both systematic uncertainties and run-to-run variability is less than 10%.

Periods with abnormal operating conditions are vetoed prior to accumulation into the averaged spectra. To verify the control system lock to a stable fringe offset, the low frequency photocurrent is continuously monitored and periods of lock loss are rejected. Periods of enhanced RF noise exceeding shot noise by 20% are also rejected. Fast noise glitches are identified by a threshold veto on the raw time-series photocurrent data. During transition periods when the control system lock of the interferometer is lost or is being reacquired, 4 seconds of frames immediately before the lock loss and immediately after a lock reacquisition are vetoed. During active data-taking, the duty cycle for stable operations is greater than 80%.

To monitor the stability of the cross-correlation data acquisition system, LED flashers placed near the output ports of each interferometer produce an in situ correlated amplitude signal at 13 MHz. The flasher signal amplitude and phase coherence in each detector is continuously recorded and indicate that the electronically isolated digitizers have high phase stability for frequencies up to 25 MHz.

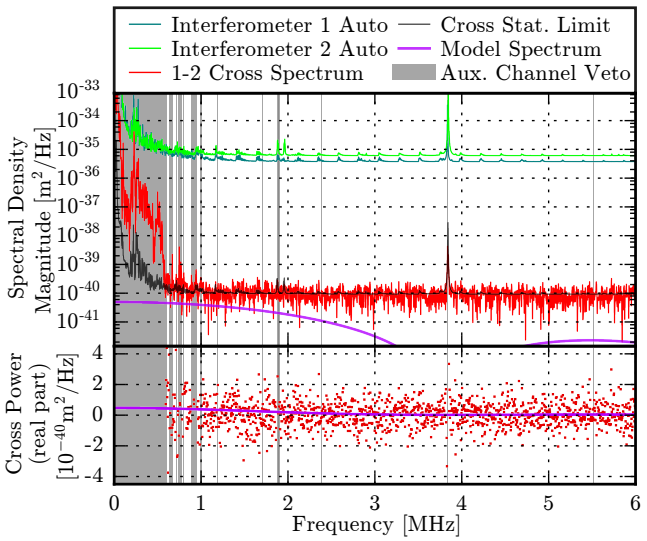

FIG. 2: Accumulated power spectra with 3.8 kHz resolution. In the upper panel, the two upper curves show the output PSD (averaged over the two photodetectors) for each interferometer. Below that are two curves showing the expected noise in the cross correlation based on $\sqrt{N}$ averaging of the PSDs, and the observed magnitude of the cross correlation data. The lower panel plot is on a linear scale and is the real part of the cross correlation spectrum. This is the signal integrated in Fig. 3. Both panels also show the predicted cHN spectrum.

Measured spectra — Fig. 2 shows the measured auto- and cross-spectra averaged over 145 hours of data taken in July-August, 2015. The auto-spectrum for each individual interferometer is obtained by a weighted average of its two output photodetectors, with weighting given by the instantaneous calibrated DARM sensitivity. The many subsequent measurements are also similarly weighted when summed into the average. The raw 381 Hz resolution spectra are frequency-averaged to produce spectra with 3.8 kHz resolution and negligible bin-to-bin correlation. At high frequencies, these spectra are shot-noise-limited as expected with flat regions well described by Gaussian noise. A repeating sequence of peaks is due to thermally excited acoustic modes of individual optics substrates. The magnitude of the resolved acoustic lines is consistent with that expected from the ambient temperature. Excess power is also seen at higher order mode resonances of the Fabry-Perot cavity for each interferometer and at the 3.8 MHz FSR. At these resonances, amplitude and phase noise present on the laser is no longer efficiently filtered by the cavity and leaks through to the output port. Because the interferometers use independent optics and lasers, the excess noise from these sources is uncorrelated but reduces the sensitivity of the experiment at affected frequencies.

The measured cross-spectral data are projected onto the real axis to search for correlation at zero time delay. The shot-noise-limited measured power is consistent with the expected statistical sensitivity with $\sqrt{N}$ improvement from averaging. The data are verified to be normally distributed with no statistically significant outliers. For reference the predicted spectrum of the holographic noise model is also shown on the plots of Fig. 2.

Backgrounds — In light of the null result reported here, a limited set of potential backgrounds is studied in order to constrain the possible destructive interference of these backgrounds with the cHN. The laser phase and amplitude noise spectra are measured in situ via optical pick-offs prior to injection, and recorded in the auxiliary RF channels. The cross-spectra of these channels with the interferometer output channels is calibrated using ex-situ transfer function measurements. At lower frequencies below 1 MHz, the interferometer output spectra are dominated the $1/f$ laser phase noise, incompletely suppressed by the cavity filter. Frequency bins with high coherence with the laser phase and amplitude monitors of the opposite interferometer, or with external antenna channels are vetoed for the analysis. Data below 100 kHz are vetoed due to a large environmental noise component, while the auxiliary channels enforce vetos at frequencies up to 600kHz and sporadically above that. These vetoes rely only on auxiliary channels and do not systematically bias the search for signal power from cHN. Vetoed regions are shaded in gray in the plots. For remaining bins, correlated or anti-correlated laser noise is statistically limited to be $< 3\%$ of the predicted cHN power. Furthermore, correlated RF pickup in the photoreceivers is constrained by dark noise studies to be $< 1\%$ of the cHN power.

Exclusion of the model — To optimize sensitivity to the predicted spectral shape of the cHN, each non-vetoed 3.8 kHz bin is weighted by the (predicted) signal-to-noise ratio. Fig. 3 shows this result in the form of a cumulative frequency integral of the weighted cross-spectrum signal from Fig. 2. Plotted on the upper panel of Fig. 3 is the measurement weight shown as a potential signal significance density for each frequency bin ($\sigma/\sqrt{\text{MHz}}$). The overall envelope of the significance function arises from the interferometer response to the cHN [7], normalized by the shot-noise-limited sensitivity. As discussed above, the shot noise is exceeded at some frequencies by other uncorrelated stochastic noise sources, causing dips in the expected significance density which reduce the instrument's integrated sensitivity by about 10% while causing no systematic bias. About 20% of the potential signal significance comes from frequencies below 1 MHz, 70% from frequencies between 1 and 2 MHz, and 10% from above 2 MHz. The integrated significance shows the potential for 6.2σ statistical sensitivity for detecting or rejecting the cHN model.

The lower panel of Fig. 3 shows the frequency integral of the predicted signal given in equation 1 weighted by the expected signal to noise ratio. This curve is normalized to integrate to unity with a shaded band representing the 10% calibration uncertainty. The lower curve in this plot is the corresponding integral of the weighted data points. This curve exhibits a random walk, thus indicating that the significance accumulation has no excessive contribution from any particular frequency band. The integral takes into account the small correlations between adjacent frequency bins due to apodization and sampling. The shaded vertical bands are vetoed regions as described above. The endpoint to the right of the plot is the total integrated signal and is the result of this analysis. The shaded band around the curve is the $\pm 1\sigma$ accumulated statistical uncertainty.

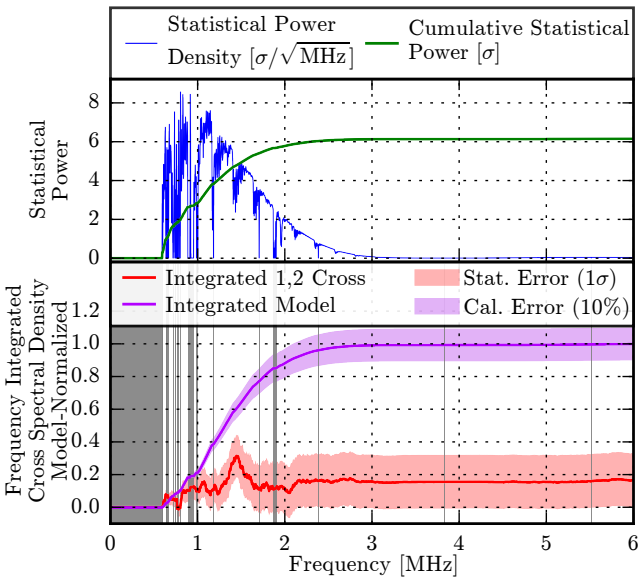

FIG. 3: The upper panel shows the predicted measurement significance (model signal/instrument noise) in each frequency bin as well as its integral. The lower panel is the frequency integrated measurement with a shaded 1σ uncertainty limit along with the integrated cHN model spectrum. Both are normalized to the predicted model amplitude. The shaded region around the model curve is the 10% calibration uncertainty. The grey bands are frequencies vetoed using ancillary and housekeeping data.

Using all data up to 25 MHz, the integral curve remains statistically consistent at 1.1σ with zero broadband correlation. The cHN model of Eq. 1 is excluded with 5.1σ statistical significance, reduced by the 10% calibration uncertainty to 4.6σ. Alternatively, the result may be viewed as a constraint on the normalization of this model to be less than 44% of the predicted value at 95% confidence level.

Conclusions — The result reported here demonstrates the viability of a new kind of experimental program to probe Planck scale physics. Concrete experimental results from experiments of this type are informative, even if they are for now only upper bounds on exotic effects po-

tentially arising from Planck scale microphysics. Further studies will survey with improved sensitivity other possible correlations with holographic information content accessible to the the current instrument[6]. These measurements will also provide uniquely deep constraints on gravitational waves in the MHz band. While the apparatus in its current Michelson layout would not respond to correlated exotic noise power in rotational observables, these could be studied with a similar instrument reconfigured as a pair of Sagnac interferometers [8].

This work was supported by the Department of Energy at Fermilab under Contract No. DE-AC02-07CH11359 and the Early Career Research program (FNAL FWP 11-03), and by grants from the John Templeton Foundation; the National Science Foundation (PHY-1205254, DGE-0909667, DGE-0638477, DGE-1144082), NASA (NNX09AR38G), the Fermi Research Alliance, the Ford Foundation, the Kavli Institute for Cosmological Physics, and University of Chicago/Fermilab Strategic Collaborative Initiatives. The Holometer team gratefully acknowledges the extensive support and contributions of Bradford Boonstra, Benjamin Brubaker, Marcin Burdzy, Herman Cease, Tim Cunneen, Steve Dixon, Bill Dymond, Jose Gallegos, Hank Glass, Emily Griffith, Gaston Gutierrez, Evan Hall, Sten Hansen, Young-Kee Kim, Mark Kozlovsky, Dan Lambert, Scott McCormick, Erik Ramberg, Geoffrey Schmit, Alex Sippel, Jason Steffen, Sali Sylejmani, Jim Volk, William Wester, and James Williams towards the design and construction of the apparatus.

[1] C. Rovelli, *Quantum gravity* (Cambridge University Press, Cambridge, UK New York, 2004).
[2] T. Jacobson, Phys. Rev. Lett. **75**, 1260 (1995).
[3] A. G. Cohen, D. B. Kaplan, and A. E. Nelson, Phys. Rev. Lett. **82**, 4971 (1999).
[4] T. Padmanabhan, Gen. Rel. Grav. **46**, 1673 (2014), 1312.3253.
[5] C. J. Hogan, Phys. Rev. **D85**, 064007 (2012).
[6] C. J. Hogan and O. Kwon (2015), arXiv:1506.06808.
[7] O. Kwon and C. J. Hogan, ArXiv e-prints (2014), 1410.8197.
[8] C. Hogan (2015), arXiv:1509.07997.
[9] R. Weiss, Quarterly Progress Report of the Research Laboratory of Electronics of the Massachusetts Institutue of Technology **105**, 54 (1972).
[10] P. Saulson, *Fundamentals of Interferometric Gravitational Wave Detectors* (World Scientific, 1994), ISBN 9810218206.
[11] The LIGO Scientific Collaboration, Rep. Prog. Phys. **72**, 076901 (2009).
[12] R. X. Adhikari, Rev. Mod. Phys. **86**, 121 (2014).
[13] W. Winkler, K. Danzmann, H. Grote, M. Hewitson, S. Hild, J. Hough, H. Lück, M. Malec, A. Freise, K. Mossavi, et al., Optics Communications **280**, 492 (2007).
[14] R. W. P. Drever, J. L. Hall, F. V. Kowalski, J. Hough, G. M. Ford, A. J. Munley, and H. Ward, Appl. Phys. B **31**, 97 (1983).
[15] E. D. Black, Am. J. Phys. **69**, 79 (2000).